# $^{60}$Coγ activation of *Cladophora rupestris* biomass functional groups and its effect on $Pb^{2+}$ adsorption

**Lu-sheng Zhang**
Anhui Agricultural University
**Zhao-wen Liu**
Anhui Agriculture University: Anhui Agricultural University
**Chang-fa Qiu**
Anhui Agriculture University: Anhui Agricultural University
**Xiao-yu Feng**
Anhui Agriculture University: Anhui Agricultural University
**Shi-ying Ma**
Anhui Agriculture University: Anhui Agricultural University
**Qian Yin**
Anhui Agriculture University: Anhui Agricultural University
**deju Cao**
cdj@ahau.edu.cn

Anhui Agricultural University https://orcid.org/0000-0003-0911-0006

**Research Article**

**Keywords:** 60Coγ-ray, C. rupestris, Pb2+, Adsorption, Functional groups, Remediation potential

**Posted Date:** December 4th, 2024

**DOI:** https://doi.org/10.21203/rs.3.rs-5103068/v1



**Version of Record:** A version of this preprint was published at Environmental Science and Pollution Research on December 26th, 2024. See the published version at https://doi.org/10.1007/s11356-024-35802-5.

# Abstract

To investigate the modification of $Pb^{2+}$ adsorption of the functional groups of *Cladophora rupestris* (*C. rupestris*) biomass by gamma radiation ($^{60}$Coγ-ray), the interface structure, chemical properties, adsorption behaviors, and $Pb^{2+}$ adsorption mechanisms of *C. rupestris* biomass were investigated after irradiation with varying doses of $^{60}$Coγ-ray. The results indicate that $^{60}$Coγ-ray significantly changed the surface characteristics and interfacial chemistry of the *C. rupestris* biomass .This led to fracturing and fragmentation that produced a larger specific surface area and more abundant pore structure, increasing the electronegativity in the *C. rupestris* biomass. The theoretical $Pb^{2+}$ adsorption capacity increased significantly (2.6–2.9 times) after $^{60}$Coγ-ray irradiation. $^{60}$Coγ-ray caused preferential degradation of protein components in the dissolved organic matter of the *C. rupestris* biomass, and protein deamination increased the absorption sites of cations. In the *C. rupestris* biomass, $^{60}$Coγ-ray altered the elemental composition and functional groups, particularly the carbon- and oxygen-containing functional groups, to improve $Pb^{2+}$ adsorption. In conclusion, $^{60}$Coγ-ray can activate the functional groups of *C. rupestris* biomass and improve their $Pb^{2+}$ adsorption sites. This study provides new insight into modification of biomass materials for enhanced removal of heavy metals from waterbodies.


# 1. Introduction

Heavy metals (HMs) have attracted widespread attention (Godoy et al. 2019) because of their toxicity and increased presence in waterbodies. $Pb^{2+}$, known for its bioaccumulation and non–degradability, is one of the most toxic HMs (Huang et al. 2023; Yang et al. 2014; Yuan et al. 2021), and the amount of $Pb^{2+}$ discharged into water systems in China increases every year (Wang et al. 2019). $Pb^{2+}$ contamination is a serious threat to human health and the environment (Yang et al. 2014).

$Pb^{2+}$ can be removed from water systems via ion exchange, membrane filtration, chemical precipitation, and adsorption (Cao et al. 2019; Ge et al. 2022; Miao and Li 2021; Zhang et al. 2019). The adsorption method has attracted widespread attention owing to its low cost, high efficiency, simple operation, and short treatment cycle (Miao and Li 2021; Zhang et al. 2019). Cao et al. (2015) and Zhang et al. (2019) reported that *Cladophora rupestris (C. rupestris*), which is widely distributed in natural waterbodies (Sucaldito and Camacho 2017; Zulkifly et al. 2012), presented favorable adsorption for $Pb^{2+}$ and $Cd^{2+}$. Therefore, *C. rupestris* is valuable as a biosorbent for the removal of $Pb^{2+}$ from waterbodies. The theoretical $Pb^{2+}$ adsorption capacity (Qm) of the organic frameworks of *C. rupestris* has been found to be 15.02 mg/g (Zhang et al. 2024).

Biochar has been widely used to remediate HM contamination (Wang et al. 2015). Moreover, modification of biomass materials, such as silicate-modified oil tea camellia shell-derived biochar for $Cd^{2+}$ removal, can often improve their HM absorption capacity (Cai et al. 2021). Wang et al. (2019) reported that the $Pb^{2+}$ Qm of fresh biochar at 350 and 650°C was 279.85 and 286.07 $mg \cdot g^{-1}$, respectively. Zhang et al. (2017) demonstrated that humic- and protein-like substances were involved in

$Pb^{2+}$ adsorption, and Wang et al. (2022) demonstrated that biochar can enhance $Pb^{2+}$ adsorption through the cosorption of dissolved organic matter (DOM). Simultaneously, ultraviolet (UV) irradiation can promote the generation of new oxidation functional groups (Wang et al. 2023). Ethylenediamine-modified pectins have exhibited a remarkable removal efficiency for $Pb^{2+}$ (Liang et al. 2020).

Gamma radiation (γ-ray) is considered an effective physical method for modifying biomass materials by engaging in cross-linking, grafting, copolymerization, and disintegration processes (Choi and Kim 2013). Mohamed et al. (2022) showed that $^{60}$Coγ-ray could improve the surface characteristics of clay minerals, enhancing the efficient removal of $Gd^{3+}$ and $Ce^{3+}$, with the primary mechanism being radical chemistry (Han et al. 2022). Zhao et al. (2022) found that polyisoprene underwent molecular transformations upon exposure to γ-ray, generating carbonyl (C = O) and hydroxyl (O − H) groups, and polyisoprene irradiated with 100 kGy of $^{60}$Coγ-ray caused the fracture of the carbon main chain and oxidation of the side-chain functional groups. Li et al. (2022) found that higher $^{60}$Coγ-ray doses can degrade the dietary fiber of a navel orange, rupturing the crystalline part of the fiber and breaking the covalent bonds. According to Gewert et al. (2018) and Wen et al. (2022), $^{60}$Coγ-ray can break the main chain of polymers, and the chemical bonds of DOM can be broken and recombined, thus changing the structural characteristics of the DOM of *C. rupestris*.

In this study, to investigate the interface structure, chemical properties, and functional group activation of *C. rupestris* biomass irradiated by $^{60}$Coγ-ray, *C. rupestris* biomass samples were treated with different $^{60}$Coγ-ray doses (0, 20, 100, and 200 kGy). $Pb^{2+}$ adsorption characteristics were investigated to reveal the $Pb^{2+}$ adsorption mechanism of *C. rupestris* biomass irradiated by $^{60}$Coγ-ray. This study provides new insight into modification of biomass materials for enhanced removal of HMs from waterbodies.

## 2. Materials and methods

## 2.1. Materials and reagents

*C. rupestris* biomass samples were collected from Heichiba in Hefei city, Anhui, China. The *C. rupestris* samples were washed with running water, dried in an oven at 60 ℃ for 24 h to constant weight, and then crushed through a 100-mesh sieve.

The lead nitrate ($Pb(NO_3)_2$) was analytical purity grade and obtained from Sinopharm Chemical Reagent Co., Ltd. (Shanghai, China). All reagents were analytical purity grade, and solutions were prepared with ultrapure water (18.25 MΩ•cm).

## 2.2. $^{60}$Coγ-ray irradiation

The *C. rupestris* biomass samples were irradiated with $^{60}$Coγ-ray doses of 0, 20, 100, and 200 kGy (Furui High Energy Technology Co., Ltd, Guangzhou, China). The samples were stored in sealed brown glass bottles.

## 2.3. Materials characterization

Surface morphology changes were observed by scanning electron microscopy (SEM; s–4800, Hitachi, Japan). The particle size distribution and specific surface area were measured by a laser particle size distributor (BT–9300H, Bettersize, China). Surface hydrophilicity was measured by a contact angle analyzer (DSA100, KRUSS, Hamburg, Germany). Surface electronegativity was measured by a zeta potential analyzer (Zetasizer Nano ZS90, Malvern, UK). Crystalline phase and crystallinity were analyzed by X-ray diffraction (XRD; D8 ADVANCE, Bruker, Germany). Functional groups were characterized by Fourier transform infrared spectroscopy (FTIR; Nicolette 50, Thermo Scientific, USA). The chemical composition of the DOM was analyzed by a three-dimensional fluorescence spectrophotometer (3D–EEM; f–4500, Horiba, Japan) and UV-visible spectrophotometer (UV-Vis; UV–1452, Shimazu, Japan). The active centers and chemical states before and after $Pb^{2+}$ adsorption were characterized by X-ray photoelectron spectroscopy (XPS; Escalab 250, Thermo–VG Scientific, USA). The specific experimental steps are presented in Supplementary Information S1.

## 2.4. Batch adsorption experiments

Adsorption isotherm experiments were performed at the initial $Pb^{2+}$ concentrations of 0, 25, 50, 100, 150, 200, 300, and 400 mg/L with a 4 g/L solid-to-liquid ratio in a 180 rpm thermostatic oscillator at 25 ℃ for 24 h. The mixtures were filtered with a 0.45 μm syringe filter, and the concentrations of $Pb^{2+}$ in the supernatant were analyzed by a flame atomic absorption spectrophotometer (ZEEnit 700P, Analytic Jena, Germany). The experiments were performed three times.

## 2.5. Environmental factors

## 2.5.1 pH

The *C. rupestris* biomass of 0.100 g treated with different $^{60}$Coγ-ray irradiation doses were added to 25 mL of $Pb^{2+}$ solution at a concentration of 400 mg/L, and the pH of the mixtures was adjusted by 0.1 M $HNO_3$ and 0.1 M NaOH to 2, 3, 4, 5, and 6 using a similar experimental step with adsorption isotherms.

## 2.5.2 Metal ion competition

The *C. rupestris* biomass of 0.100 g treated with different $^{60}$Coγ-ray irradiation doses were added to 25 mL of a solution containing 50 mg/L solution of $Pb^{2+}$, $Cd^{2+}$, $Cu^{2+}$, $Zn^{2+}$, and $Ni^{2+}$ to analyze the Qm of the *C. rupestris* biomass to different HM ions.

## 2.6 Release of net alkali metal cations and reusability

The $K^+$, $Na^+$, $Ca^{2+}$, and $Mg^{2+}$ concentrations were determined in pure water and in a 400 mg/L $Pb^{2+}$ solution, and the water-soluble $K^+$, $Na^+$, $Ca^{2+}$, and $Mg^{2+}$ contents were calculated per unit of the biomass (Shen et al. 2017). After the equilibrium of adsorption, the sample was repeatedly centrifuged and

filtered with ultrapure water for 3 times, and then 0.1 M dilute hydrochloric acid was added for resolution for 24 h, and the cycle was repeated for 4 times.

## 2.7. Data analysis

The adsorption isotherms were fitted using the Langmuir and Freundlich models (details in Supplementary Information S2). The experimental data were analyzed and graphed using SPSS 22.0 and Origin2018, and the Duncan method was used for the significant difference comparison ($p < 0.05$).

# 3. Results and discussion

## 3.1. Characteristics of *C. rupestris* biomass irradiated by $^{60}$Coγ-rays

### 3.1.1. Morphology, particle size, and crystallinity

The surface morphology of the *C. rupestris* biomass treated with different $^{60}$Coγ-ray irradiation doses is shown in Fig. 1. The *C. rupestris* biomass samples were rough and full of grooves, with particles attached. However, cracks were gradually generated on the surface of the *C. rupestris* biomass samples treated with $^{60}$Coγ-ray irradiation and pores tended to develop on the interior surface of the samples. Notably, with increasing $^{60}$Coγ-ray irradiation doses, the surface morphology of the *C. rupestris* biomass samples changed more drastically, showing voids, increased tiny pores on the smooth surface, and an irregular structure. Overall, $^{60}$Coγ-ray increased the specific surface area of the *C. rupestris* biomass samples, and more developed pore structures were observed at higher $^{60}$Coγ-ray irradiation doses.

The particle size distribution of the *C. rupestris* biomass treated with $^{60}$Coγ-ray is shown in Fig. 2a. As the $^{60}$Coγ-ray irradiation dose increased from 0 to 200 kGy, the median diameter (D50) of the particle decreased from 52.26 to 39.73 μm, respectively. The drop ratio was 23.98% when the $^{60}$Coγ-ray irradiation dose was 200 kGy. The specific surface area of the *C. rupestris* biomass samples treated with $^{60}$Coγ-ray increased 14.6% from 159.1 to 182.3 $m^2$/kg at radiation doses of 0 to 200 kGy, respectively, indicating that $^{60}$Coγ-ray can cause fracture and breakage, creating a larger surface area that can be conducive to activate relevant functional groups (Zhu et al. 2019). These findings are similar to those of Mohamed et al. (2022).

The XRD spectra are shown in Fig. 2b. The peak intensity at 2θ values of 29.76°, 39.76°, 47.78°, and 48.89°, which is known as $CaCO_3$ (Miao and Li 2021), was significantly increased, particularly the 2θ value of 29.76°. This increase was more evident as the irradiation dose increased, indicating that the crystallinity and brittleness of the *C. rupestris* biomass increased with increasing $^{60}$Coγ-ray irradiation doses (Xue et al. 2023), and the *C. rupestris* biomass were easier to break and fracture (Shen et al. 2023). The XRD spectra show that $^{60}$Coγ-ray led to the *C. rupestris* biomass having an amorphous

structure and their experiencing the breakage of the main polymer chain, which contributed to its crystallinity (Shen et al. 2023). This result is consistent with the particle size analysis result.

Therefore, $^{60}$Coγ-ray can cause the fracture and fragmentation of *C. rupestris*, resulting in a reduction in particle size and an increase in specific surface area, which can increase its HM-ion adsorption potential.

## 3.1.2. Zeta potentials and functional groups

Figure 2c displays the zeta potentials of the *C. rupestris* biomass with pH values in the range of 2–9. With increasing $^{60}$Coγ-ray irradiation doses, the electronegativity of the *C. rupestris* biomass s increased, indicating that $^{60}$Coγ-ray causes *C. rupestris* biomass to attract electrons and become negatively charged (Liang et al. 2020). In summary, $^{60}$Coγ-ray significantly increased the electronegativity of *C. rupestris* biomass. The increased electronegativity might increase the adsorption of cations owing to the reduced electrostatic repulsion between the adsorbent and cations.

The FTIR results of the *C. rupestris* biomass samples treated with $^{60}$Coγ-ray are shown in Fig. 2d. The deformation vibration of the aromatic $CH_2$ peak at 1428.53 $cm^{-1}$ (Godoy et al. 2019) and bending vibration of the aromatic C − H peaks at 876.02 and 712.73 $cm^{-1}$ (Tan et al. 2020; Yang et al. 2014) significantly decreased as the $^{60}$Coγ-ray irradiation dose increased, indicating that $^{60}$Coγ-ray induced the benzene-ring breakage of *C. rupestris* biomass (Li et al. 2022). The peaks at 2924.76 and 2858.10 $cm^{-1}$ (Guan et al. 2020), corresponding to the symmetric and symmetric stretching vibrations of aliphatic C − H, respectively, decreased (Zhu et al. 2019), implying the cleavage of the C − H and C − C bonds from the main polymer chain. The stretching vibration of O − H at 3374.38 $cm^{-1}$ (Zhang et al. 2017) was enhanced and blue shifted, indicating the impact of different irradiation treatments on the structure of hydrogen and the hydroxyl group in cellulose and hemicelluloses (Li et al. 2022). The intensity of the C = O characteristic peak at 1647.89 $cm^{-1}$ (Liu et al. 2019), the position and peak shape of the asymmetric stretching vibration and symmetric stretching vibration of C − O−C at 1161.41 and 1110.30 $cm^{-1}$(Chen et al. 2015), and the stretching vibration of C − O−H at 1034.61 $cm^{-1}$ all shifted accordingly after $^{60}$Coγ-ray irradiation. These results demonstrate that oxidation reactions occurred with $^{60}$Coγ-ray irradiation that caused a series of complex chain expansions, branching, and chain termination, and eventually led to the formation of C = O, C − O−C, and C − O−H (Zhu et al. 2019). The peaks at 1579.18 $cm^{-1}$ for C − N and N − H showed marked shoulder peaks after $^{60}$Coγ-ray irradiation, indicating that more amide functional groups were generated (Guan et al. 2020). This result is consistent with that of Wang et al. (2023), who found that C = O and O − H can be formed by UV irradiation. The results are also consistent with those of Zhu et al. (2022) who found that high-dose irradiation of $^{60}$Coγ-ray can significantly destroy the structure of lignocellulose.

In conclusion, $^{60}$Coγ-ray can alter the elemental composition and functional groups of *C. rupestris* biomass, especially in carbon- and oxygen-containing functional groups (CFGs and OFGs).

## 3.1.3. Hydrophilicity

The water contact angle is used to characterize the hydrophobicity of a material, and the larger the contact angle, the more hydrophobic the material (Hu et al. 2023). The hydrophilicity was enhanced, and the adsorption amounts of $Pb^{2+}$ and $Cu^{2+}$ increased after microplastic aging (Wang et al. 2023). Figure 3a shows that the water contact angle of the *C. rupestris* biomass decreased from 99.7° to 87.2° a$^{60}$Coγ-ray irradiation doses increased from 0 to 200 kGy, respectively, indicating that the hydrophilicity of *C. rupestris* biomass increased. $^{60}$Coγ-ray irradiation can produce hydrophilic groups, which enhances the $Pb^{2+}$ adsorption efficiency (Wang et al. 2023; Liu et al. 2019).

# 3.1.4. DOM

DOM can adsorb, complex, and redox HMs (Mu et al. 2022). Huang et al. (2020) reported that DOM and $Pb^{2+}$ can form soluble complexes to inhibit the adsorption and precipitation of HMs. After treating the *C. rupestris* biomass with $^{60}$Coγ-ray, the 3D-EEM fluorescence spectra of the DOM released from the *C. rupestris* biomass changed (Fig. 3b). The intensity of peak A at Ex/Em = 276–279/347–353 nm, assigned to tryptophan-like substances (Li et al. 2020; Liu et al. 2022; Teng et al. 2019), decreased significantly as the $^{60}$Coγ-ray irradiation dose increased and disappeared when the $^{60}$Coγ-ray irradiation dose reached 200 kGy. Meanwhile, peak B at Ex/Em = 336–342/422–428 nm, assigned to humic acid (HA)-like substances (Li et al. 2020; Liu et al. 2022; Teng et al. 2019), exhibited a significant red shift with $^{60}$Coγ-ray treatment, and the fluorescence intensity of the humic component increased in the DOM, especially when the irradiation dose reached 200 kGy. Therefore, $^{60}$Coγ-ray can cause degradation of protein components and cause the amino group of the protein to fall off, thus increasing the humification process of DOM (Zhang et al. 2020). Photoaging may promote the release of soluble organics (Hu et al. 2023), causing amino groups of the protein to fall off and the absorption sites of cations to increase, which might increase the $Pb^{2+}$ adsorption efficiency (Chen et al. 2020). Shi et al. (2020) demonstrated that $Pb^{2+}$ was directly adsorbed by green algae until equilibrium in the presence of HA, and $Pb^{2+}$ bound to the algae in the form of a Pb–FA conjugated copolymer (Shi et al. 2020). $Pb^{2+}$ can form ternary complexes with biodegradable microplastics and their leached HA, providing new adsorption sites for unbound $Pb^{2+}$, thus enhancing the Qm for $Pb^{2+}$ (Li et al. 2022).

In conclusion, $^{60}$Coγ-ray caused preferential degradation of protein components in the DOM of the *C. rupestris* biomass (Cao et al. 2019; Yang et al. 2014), and protein deamination increased the absorption sites of the cations.

As shown in Fig. S1a, the absorption wavelength of the DOM released from the *C. rupestris* biomass samples shifted toward the higher wavelength with an increase in the $^{60}$Coγ-ray irradiation, suggesting that $^{60}$Coγ-ray caused the oxidation of the DOM (Gao et al. 2021). The absorption peaks of the UV-Vis spectra at 250–290 nm represent heterocyclic aromatic hydrocarbons, and 390 nm represents the carbonyl or conjugated groups (Teng et al. 2021). Fig. S1a shows that the UV-Vis spectra at 281 nm were blue shifted to 269 nm, suggesting that $^{60}$Coγ-ray caused the heterocyclic aromatic hydrocarbons to change in the DOM and indicating that the π–π* electron transition of algae-derived DOM decreased with

increasing irradiation doses (Janot et al. 2010). The spectra at 400 nm were blue shifted to 390 nm, indicating that carbonyl or conjugated groups were produced by $^{60}$Coγ-ray irradiation and $^{60}$Coγ-ray had some effect on the polyene structure containing seven conjugated double bonds in the visible region of the algae-derived DOM (Klempová et al. 2023; Zhou et al. 2020).

In conclusion, $^{60}$Coγ-ray causes successive decomposition and transformation of DOM, altering the molecular configuration of DOM (Dryer et al. 2008).

## 3.2. Adsorption of $Pb^{2+}$ onto *C. rupestris* biomass

### 3.2.1. Qm

The Langmuir and Freundlich isotherms of $Pb^{2+}$ on the *C. rupestris* biomass treated with different doses of $^{60}$Coγ-ray irradiation are shown in Fig. 4. The theoretical $Pb^{2+}$ Qm of the *C. rupestris* biomass increased significantly to 74.907, 79.800, and 82.550 mg/g after $^{60}$Coγ-ray irradiation doses of 20, 100, and 200 kGy, respectively, with an increase of 2.6–2.9 times. After $^{60}$Coγ-ray irradiation, the $Pb^{2+}$ adsorption of the *C. rupestris* biomass showed a linear growth trend at equilibrium concentrations (Ces) in the range of 0–40 mg/L and then became saturated when Ce ≥ 40 mg/L. This may be attributed to $^{60}$Coγ-ray, which increases the adsorption sites and functional groups and reduces the spatial site resistance, thus significantly increasing the equilibrium Qm (Spessato et al. 2019).

The fitting parameters of the Langmuir and Freundlich models are listed in Table 1. The adsorption isotherms were well fit by the Langmuir and Freundlich models ($R^2 \geq 0.92$) when the $^{60}$Coγ-ray irradiation dose was lower than 100 kGy; subsequently, the $R^2$ dropped significantly, particularly in the Freundlich model ($R^2 = 0.70$) at 200 kGy, which indicates that the Freundlich model was unable to describe the adsorption characteristics in the analyzed cases. The $K_L$ values of the Langmuir model decreased as the $^{60}$Coγ-ray irradiation dose increased, indicating that the adsorption process was not a single surface chemisorption but was also affected by other forces (Li et al. 2020; Martins et al. 2015). Liu et al. (2019) found that the surface of UV-aged microplastics is rougher and has some cracks. The high energy of $^{60}$Coγ-ray can allow oxidation to occur in the deeper layers, which leads to enhanced chemisorption (Huang et al. 2020; Teng et al. 2019; Zhang et al. 2020). The Freundlich constant $K_f$—free energy of adsorption—indicates the lative biosorption capacity of the biosorbent bonding energy. In this study, $K_f$ was 1.48–10.72, which reflects the high affinity of $Pb^{2+}$ to the binding sites of the *C. rupestris* biomass (Pillai et al. 2013), especially at the $^{60}$Coγ-ray irradiation dose of 200 kGy. The slope 1/n in the Freundlich model was less than 1, indicating that $^{60}$Coγ-ray irradiation increased the surface heterogeneity of the *C. rupestris* biomass(Xie et al. 2015).

Table 1
Adsorption isotherm parameters of the Langmuir and Freundlich models

| Irradiation treatment | Model parameters | | | | | |
|---|---|---|---|---|---|---|
| | Langmuir | | | Freundlich | | |
| | $K_L$/L•mg$^{-1}$ | Qm/mg•g$^{-1}$ | $R^2$ | $K_f$ mg$^{1-1/n}$•g$^{-1}$•L$^{1/n}$ | 1/n | $R^2$ |
| 0 kGy | 0.808 | 30.383 | 0.924 | 9.43 | 0.272 | 0.981 |
| 20 kGy | 0.137 | 74.907 | 0.965 | 7.85 | 0.494 | 0.943 |
| 100 kGy | 0.125 | 79.800 | 1.000 | 7.48 | 0.494 | 0.999 |
| 200 kGy | 0.167 | 82.550 | 0.842 | 10.72 | 0.439 | 0.696 |

In conclusion, $^{60}$Coγ-ray irradiation decreases the free energy of adsorption, increasing the biosorption capacity and affinity of $Pb^{2+}$ to the binding sites of *C. rupestris* biomass.

## 3.2.2. Influence of pH

The influence of pH on the $Pb^{2+}$ adsorption capability of the *C. rupestris* biomass is shown in Fig. 5a. The $Pb^{2+}$ adsorption capability of the *C. rupestris* biomass increased as the pH increased, and the $Pb^{2+}$ Qm increased to 19.04 mg/g when the pH was 6. This trend can be attributed to the increased dissolution of insoluble crystalline minerals in low pH environments, which releases a large number of cations ($H^+$, $K^+$, $Na^+$, $Ca^{2+}$, and $Mg^{2+}$) that can compete with $Pb^{2+}$ for adsorption sites, leading to a decrease in $Pb^{2+}$ adsorption (Wang et al. 2022). As the solution pH increased, deprotonation of the functional groups led to the formation of negative charges, facilitating cation adsorption through electrostatic interactions (Liang et al. 2020). After $^{60}$Coγ-ray irradiation, the pH had no significant effect on the $Pb^{2+}$ adsorption.

The above phenomena indicate that *C. rupestris* biomass has better environmental adaptability to $Pb^{2+}$ after $^{60}$Coγ-ray irradiation (Yang et al. 2014)—consistent with the results of the zeta potential analysis.

## 3.2.3. Competitive adsorption of other HM ions

The competitive adsorption of the *C. rupestris* biomass is shown in Fig. 5b. There was a significant difference for the different HMs, and the order of Qm was $Pb^{2+} > Cd^{2+} > Ni^{2+} \approx Zn^{2+} > Cu^{2+}$, implying preferential adsorption of $Pb^{2+}$. These results are similar to those of Cao et al. (2015), in which *C. rupestris* was found to be able to accumulate $Pb^{2+}$. Zhang et al. (2019) suggested that *C. rupestris* has a bioremediation potential for $Cd^{2+}$. After the irradiation of $^{60}$Coγ-ray at doses of 0 to 200 kGy, the $Pb^{2+}$ Qm increased from 10.73–24.00%, respectively. The adsorption capacities of $Zn^{2+}$, $Cd^{2+}$, and $Ni^{2+}$ also improved significantly after $^{60}$Coγ-ray irradiation, but the $Cu^{2+}$ Qm did not significantly increase.

These findings suggest that $^{60}$Coγ-ray irradiation can activate the relevant adsorption sites and functional groups, and, among all the HMs tested, *C. rupestris* biomass demonstrated the highest affinity for $Pb^{2+}$. These findings are similar to those of Zhao et al. (2023).

### 3.2.4. The reusability and desorption

As shown in Fig. 6, after four desorption and regeneration cycles, the adsorption capacity of $Pb^{2+}$ on *C. rupestris* biomass samples after $^{60}$Coγ-ray irradiation only decreased by 28.25%, 17.51%, 18.97% and 15.36%. This phenomenon suggests that the adsorption capacity of the biomass is still high after several desorption and regeneration cycles (Chen et al. 2021)

## 3.3. Effect of groups activation by $^{60}$Coγ-ray and adsorption of $Pb^{2+}$

As shown in Fig. 7, 10.1 wt % Pb was detected on the *C. rupestris biomass* samples and Pb was mainly adsorbed on the surface and pores by combining with C and O.

As shown in Fig. S2 and Table S1, *C. rupestris* biomass contains a large amount of O (50.37%), C (28.12%), and Ca (19.22%), as well as a small amount of N (2.30%). The functional groups and amorphous parts have been reported to be composed of these elements can act as initiators for photodegradation (Zhu et al. 2019). The O content and O/C ratio increased with increased $^{60}$Coγ-ray irradiation doses, indicating that $^{60}$Coγ-ray can cause *C. rupestris* biomass to produce more OFGs (Hu et al. 2023). The Pb 4f characteristic peak appeared in the irradiated *C. rupestris* biomass, indicating that $Pb^{2+}$ was successfully adsorbed onto the *C. rupestris* biomass.

The C 1s peak of the *C. rupestris* biomass can be deconvoluted into four individual peaks corresponding to C−(C, H)/C = C (284.80 eV), C − O (286.20–286.73 eV), C = O (287.81–288.03 eV), and O − C = O (288.60–289.55 eV) (Zafar et al. 2022) (Fig. 8). After the irradiation of $^{60}$Coγ-ray at doses of 0 to 200 kGy, the peak intensity of C−(C, H)/C = C of the *C. rupestris* biomass decreased from 15.14–11.25%, and the peak intensity of C − O increased from 15.6 to 11.34%, respectively. This result indicates that $^{60}$Coγ-ray irradiation caused the C−(C, H) bonds to fracture and the benzene ring to open. These broken bonds are highly reactive and rapidly react with $O_2$ to form C − O bonds (Wang et al. 2023), which subsequently form C = O bonds, leading to the generation of unsaturated bonds represented by alcohols, aldehydes, and acids (Zhu et al. 2020). The C−(C, H)/C = C content in the *C. rupestris* biomass irradiated with 0 kGy of $^{60}$Coγ-ray and loaded with $Pb^{2+}$ showed the most pronounced shift of 2.61%, indicating that the aromatic structure of the *C. rupestris* biomass participated in the Pb–π interaction adsorption process (Liu et al. 2023). After being treated with $^{60}$Coγ-ray, the consumption of C − O was between 10.23% and 11.13%, indicating that the functional groups with C as the backbone underwent significant changes.

Oxygen atoms often act as electron donors to form stable covalent bonds with HMs and play a crucial role in chelation (Wu et al. 2019). The primary OFGs in the *C. rupestris* biomass were C = O and C − O

(Fig. S3). After $^{60}$Coγ-ray irradiation, the content of the C = O bonds decreased while that of the C − O bonds increased, and the ratio of C = O/C − O decreased from 1.56 to 1 for $^{60}$Coγ-ray doses of 0 to 200 kGy, respectively. The O − C = O functional group was observed when the $^{60}$Coγ-ray dose was 200 kGy, indicating that the OFGs of *C. rupestris* biomass were enhanced after $^{60}$Coγ-ray irradiation (Wu et al. 2021). The binding energy of the OFGs declined in the Pb-loaded *C. rupestris* biomass, suggesting that the chelation by the OFGs is crucial during $Pb^{2+}$ adsorption. After $^{60}$Coγ-ray irradiation, the content of the C − O bonds in the *C. rupestris* biomass loaded with $Pb^{2+}$ decreased from 12.97–9.36% for $^{60}$Coγ-ray doses of 0 to 200 kGy, respectively. Particularly, the O − C = O content of the *C. rupestris* biomass sample treated with 200 kGy of $^{60}$Coγ-ray irradiation decreased to 5.77%, indicating that O − C = O plays an important role in $Pb^{2+}$ adsorption (Chen et al. 2021). In summary, $^{60}$Coγ-ray irradiation activates the OFGs of *C. rupestris* biomass, enhancing the ability of the OFGs in *C. rupestris* biomass to bind with $Pb^{2+}$.

As shown in Fig. 9, the Pb 4f7/2 and Pb 4f5/2 spectra of the *C. rupestris* biomass samples after $^{60}$Coγ-ray irradiation can be deconvoluted into a pair of peaks corresponding to $Pb^{2+}$ and Pb − O (Wu et al. 2019). Therefore, the main combined forms of Pb were $Pb^{2+}$ and Pb − O. This phenomenon suggests that not only electrostatic interactions but also bonding interactions existed between Pb and *C. rupestris* biomass (Wu et al. 2019). The $Pb^{2+}$/Pb − O ratio changed from 1.53 to 0.85 after the irradiation of $^{60}$Coγ-ray at doses of 0 to 200 kGy, respectively, indicating that $^{60}$Coγ-ray irradiation promoted the bonding interaction between the *C. rupestris* biomass and Pb to form Pb − O.

However, the XRD results show that no Pb precipitation was generated after the adsorption of $Pb^{2+}$ (Fig. 10), indicating that precipitation was not an adsorption mechanism of $Pb^{2+}$.

## 3.4 Release of metal ions and DOM from C. rupestris biomass by $^{60}$Coγ-ray

The release of small amounts of $K^+$, $Na^+$, $Mg^{2+}$, and large amounts of $Ca^{2+}$ from the solution before and after the adsorption of $Pb^{2+}$ by the *C. rupestris* biomass samples is shown in Table S2, suggesting that $^{60}$Coγ-ray was more favorable for $Ca^{2+}$ release from the cell wall of the *C. rupestris* biomass samples (Fan et al. 2021), resulting in enhanced ion exchange between $Pb^{2+}$ and $Ca^{2+}$ (Gao et al. 2019).

After $Pb^{2+}$ adsorption, the 3D-EEM fluorescence spectra of the DOM released from the *C. rupestris* biomass decreased drastically, indicating that $^{60}$Coγ-ray caused π-electron mobility on the aromatic carbon “core” and enhanced the conjugated unsaturated structure (Fig. S4) (Qu et al. 2016). In Fig. S1b, the disappearance of the two shoulder peaks suggests the binding of $Pb^{2+}$ and the DOM. In the wavelength range > 390 nm, the absorption spectra of DOM showed almost no change, suggesting that intermolecular reaction and the molecular structure did not play a significant role in the binding of $Pb^{2+}$ and the DOM due to $^{60}$Coγ-ray (Yan et al. 2013). Therefore, the binding of $Pb^{2+}$ and the DOM was mainly

due to the interaction of the carboxylate chromophores with $^{60}$Coγ-ray (Teng et al. 2021). $^{60}$Coγ-ray caused the successive decomposition and transformation of the DOM of the *C. rupestris* biomass, and the carboxy chromophore played an important role in the reaction with $Pb^{2+}$.

In conclusion, $^{60}$Coγ-ray irradiation causes *C. rupestris* biomass to be dearomatized, which exposes more unsaturated carbon-binding sites for $Pb^{2+}$ adsorption, while *C. rupestris* biomass treated with a high $^{60}$Coγ-ray irradiation dose contain more OFGs and ion-exchange sites, which provide more active adsorption sites for $Pb^{2+}$ (Li et al. 2018).

# 4. Conclusions

(1) $^{60}$Coγ-ray significantly changed the surface characteristics and interfacial chemistry of the *C. rupestris* biomass, causing fracturing and fragmentation, producing a larger specific surface area and more abundant pore structure, and increasing the electronegativity.

(2) The theoretical $Pb^{2+}$ Qm of the *C. rupestris* biomass increased significantly (2.6–2.9 times) after $^{60}$Coγ-ray irradiation. $^{60}$Coγ-ray irradiation can activate the relevant adsorption sites and increase the $Pb^{2+}$ affinity of *C. rupestris* biomass.

(3) $^{60}$Coγ-ray caused preferential degradation of protein components in the DOM of the *C. rupestris* biomass, and protein deamination increased the absorption sites of cations.

(4) $^{60}$Coγ-ray altered the elemental composition and functional groups of the *C. rupestris* biomass, especially the carbon-containing functional groups and OFGs. $^{60}$Coγ-ray irradiation activated the OFGs of the *C. rupestris* biomass, promoting the adsorption of $Pb^{2+}$.

(5) $^{60}$Coγ-ray irradiation produced a high degree of dearomatization, which exposed more unsaturated carbon-binding adsorption sites for $Pb^{2+}$. The *C. rupestris* biomass treated with a high $^{60}$Coγ-ray irradiation dose of 200 kGy contained more OFGs and ion-exchange sites, which provided more active $Pb^{2+}$ adsorption sites.

These findings indicate that irradiation of $^{60}$Coγ-ray is an efficient technique for improving the $Pb^{2+}$ adsorption of *C. rupestris* biomass, aiding in enhanced removal of HMs from waterbodies.

# Declarations

### Ethical Approval

Not applicable.

### Consent to Participate

We consent to participate this manuscript.

### Consent to Publish

We consent to publish this manuscript.

### Authors Contributions

Lu-sheng Zhang: Methodology, Writing - original draft, Investigation. Zhao-wen Liu and Chang-fa Qiu: Software, Formal analysis. Xiao-yu Feng: Conceptualization, Software. Shi-ying Ma and Qian Yin: Visualization, Conceptualization. De-ju Cao: Resources, Writing - review & editing, Supervision, Data curation.


### Funding

This work was supported by the Natural Science Foundation of China (41877418) and the financial aid of Nature Fund of Anhui Province of China (1808085MD100).


### Competing Interests

The authors declare that they have no conflict of interest.

### Availability of data and materials

We declared that the data and materials presented in this paper are reliable.

## References


1. Cai T, Liu X, Zhang J, Tie B, Lei M, Wei X, Peng O, Du H (2021) Silicate-modified oiltea camellia shell-derived biochar: A novel and cost-effective sorbent for cadmium removal. J Clean Prod 281:125390. https://doi.org/10.1016/j.jclepro.2020.125390.
2. Cao DJ, Shi XD, Li H, Xie PP, Zhang HM, Deng JW, Liang YG (2015) Effects of lead on tolerance, bioaccumulation, and antioxidative defense system of green algae, Cladophora. Ecotoxicol Environ. Saf 112:231–237. https://doi.org/10.1016/j.ecoenv.2014.11.007.
3. Cao Y, Xiao W, Shen G, Ji G, Zhang Y, Gao C, Han L (2019) Carbonization and ball milling on the enhancement of Pb (II) adsorption by wheat straw: Competitive effects of ion exchange and precipitation. Bioresour Technol 273:70–76. https://doi.org/10.1016/j.biortech.2018.10.065.
4. Chen CC, Zhu X, Xu H, Chen F, Ma J, Pan K (2021) Copper adsorption to microplastics and natural particles in seawater: A comparison of kinetics, isotherms, and bioavailability. Environ Sci Technol 55:13923–13931. https://doi.org/10.1021/acs.est.1c04278.
5. Chen W, Peng L, Hu K, Zhang Z, Peng C, Teng C, Zhou K (2020) Spectroscopic response of soil organic matter in mining area to Pb/Cd heavy metal interaction: A mirror of coherent structural variation. J Hazard Mater 393:122425. https://doi.org/10.1016/j.jhazmat.2020.122425.

6. Chen Z, Xiao X, Chen B, Zhu L (2015) Quantification of chemical states, dissociation constants and contents of oxygen-containing groups on the surface of biochars produced at different temperatures. Environ Sci Technol 49:309–317. https://doi.org/10.1021/es5043468.
7. Choi J, Kim H.-J (2013) Preparation of low molecular weight fucoidan by gamma-irradiation and its anticancer activity. Carbohydr Polym 97:358–362. https://doi.org/10.1016/j.carbpol.2013.05.002.
8. Dryer DJ, Korshin GV, Fabbricino M (2008) In situ examination of the protonation behavior of fulvic acids using differential absorbance spectroscopy. Environ Sci Technol 42:6644–6649. https://doi.org/10.1021/es800741u.
9. Fan X, Ma Z, Zou Y, Liu J, Hou J (2021) Investigation on the adsorption and desorption behaviors of heavy metals by tire wear particles with or without UV ageing processes. Environ Res 195:110858. https://doi.org/10.1016/j.envres.2021.110858.
10. Gao LY, Deng JH, Huang GF, Li K, Cai KZ, Liu Y, Huang F (2019) Relative distribution of Cd2+ adsorption mechanisms on biochars derived from rice straw and sewage sludge. Bioresour Technol 272:114–122. https://doi.org/10.1016/j.biortech.2018.09.138.
11. Gao Y, Li N, Li J, Du B, Liu Z (2021) Charge transport behavior in gamma-ray irradiated poly (ethylene terephthalate) estimated by surface potential decay. High Volt 6:435–447. https://doi.org/10.1049/hve2.12037.
12. Ge Q, Tian Q, Wang S, Zhang J, Hou R (2022) Highly efficient removal of lead/cadmium by phosphoric acid-modified hydrochar prepared from fresh banana peels: Adsorption mechanisms and environmental application. Langmuir 38:15394–15403. https://doi.org/10.1021/acs.langmuir.2c02693.
13. Gewert B, Plassmann M, Sandblom O, MacLeod M (2018) Identification of chain scission products released to water by plastic exposed to ultraviolet light. Environ Sci Technol Letters 5:272–276. https://doi.org/10.1021/acs.estlett.8b00119.
14. Godoy V, Blázquez G, Calero M, Quesada L, Martín-Lara MA (2019) The potential of microplastics as carriers of metals. Environ Pollut 255:113363. https://doi.org/10.1016/j.envpol.2019.113363.
15. Guan J, Qi K, Wang J, Wang W, Wang Z, Lu N, Qu J (2020) Microplastics as an emerging anthropogenic vector of trace metals in freshwater: Significance of biofilms and comparison with natural substrates. Water Res 184:116205. https://doi.org/10.1016/j.watres.2020.116205.
16. Han Z, Zhu H, Cheng JH (2022) Structure modification and property improvement of plant cellulose: Based on emerging and sustainable nonthermal processing technologies. Food Res Int 156:111300. https://doi.org/10.1016/j.foodres.2022.111300.
17. Hu J, Lim FY, Hu J (2023) Characteristics and behaviors of microplastics undergoing photoaging and Advanced Oxidation Processes (AOPs) initiated aging. Water Res 232:119628. https://doi.org/10.1016/j.watres.2023.119628.
18. Huang M, Li Z, Chen M, Wen J, Luo N, Xu W, Ding X, Xing W (2020) Dissolved organic matter released from rice straw and straw biochar: Contrasting molecular composition and lead binding behaviors. Sci Total Environ 739:140378. https://doi.org/10.1016/j.scitotenv.2020.140378.

19. Huang W, Deng J, Liang J, Xia X (2023) Comparison of lead adsorption on the aged conventional microplastics, biodegradable microplastics and environmentally-relevant tire wear particles. Chem Eng J 460:141838. https://doi.org/10.1016/j.cej.2023.141838.
20. Janot N, Reiller PE, Korshin GV, Benedetti MF 44 (2010) Using spectrophotometric titrations to characterize humic acid reactivity at environmental concentrations, Environ Sci Technol 44:6782–6788. https://doi.org/10.1021/es1012142.
21. Klempová S, Oravec M, Vizárová K (2023) Analysis of thermally and UV–Vis aged plasticized PVC using UV–Vis, ATR-FTIR and Raman spectroscopy, Spectrochim. Acta A Mol Biomol Spectrosc 294:122541. https://doi.org/10.1016/j.saa.2023.122541.
22. Li H, Zhang T, Tsang DC, Li G (2020) Effects of external additives: Biochar, bentonite, phosphate, on co-composting for swine manure and corn straw. Chemosphere 248:125927. https://doi.org/10.1016/j.chemosphere.2020.125927.
23. Li X, Wang B, Hu W, Chen H, Sheng Z, Yang B, Yu L (2022) Effect of γ-irradiation on structure, physicochemical property and bioactivity of soluble dietary fiber in navel orange peel. Food Chem.: X 14:100274. https://doi.org/10.1016/j.fochx.2022.100274.
24. Li Y, Liu X, Zhang P, Wang X, Cao Y, Han L (2018) Qualitative and quantitative correlation of physicochemical characteristics and lead sorption behaviors of crop residue-derived chars. Bioresour Technol 270:545–553. https://doi.org/10.1016/j.biortech.2018.09.078.
25. Li Y, Wang F, Miao Y, Mai Y, Li H, Chen X, Chen J (2020) A lignin-biochar with high oxygen-containing groups for adsorbing lead ion prepared by simultaneous oxidization and carbonization. Bioresour Technol 307:123165. https://doi.org/10.1016/j.biortech.2020.123165.
26. Li Y, Wang X, Wang Y, Sun Y, Xia S, Zhao J (2022) Effect of biofilm colonization on Pb (II) adsorption onto poly (butylene succinate) microplastic during its biodegradation. Sci Total Environ 833:155251. https://doi.org/10.1016/j.scitotenv.2022.155251.
27. Liang RH, Li Y, Huang L, Wang XD, Hu XX, Liu CM, Chen MS, Chen J (2020) $Pb^{2+}$ adsorption by ethylenediamine-modified pectins and their adsorption mechanisms. Carbohydr Polym 234:115911. https://doi.org/10.1016/j.carbpol.2020.115911.
28. Liu G, Zhu Z, Yang Y, Sun Y, Yu F, Ma J (2019) Sorption behavior and mechanism of hydrophilic organic chemicals to virgin and aged microplastics in freshwater and seawater. Environ Pollut 246:26–33. https://doi.org/10.1016/j.envpol.2018.11.100.
29. Liu P, Dai J, Ren H, Yang Z, Zhu C, Zhang Y, Guo X, Zhu L (2022) Wastewater preinteraction accelerates the photoaging of disposable box-derived polystyrene microplastics in water. Water Res 226:119294. https://doi.org/10.1016/j.watres.2022.119294.
30. Liu P, Qian L, Wang H, Zhan X, Lu K, Gu C, Gao S (2019) New insights into the aging behavior of microplastics accelerated by advanced oxidation processes. Environ Sci Technol 53:3579–3588. https://doi.org/10.1021/acs.est.9b00493.
31. Liu Y, Chen Y, Li Y, Chen L, Jiang H, Jiang L, Yan H, Zhao M, Hou S, Zhao C, Chen Y (2023) Elaborating the mechanism of lead adsorption by biochar: Considering the impacts of water-washing and

freeze-drying in preparing biochar. Bioresour Technol 386:129447. https://doi.org/10.1016/j.biortech.2023.129447.

32. Martins AC, Pezoti O, Cazetta AL, Bedin KC, Yamazaki DA, Bandoch GF, Asefa T, Visentainer JV, Almeida VC (2015) Removal of tetracycline by NaOH-activated carbon produced from macadamia nut shells: kinetic and equilibrium studies. Chem Eng J 260:291–299. https://doi.org/10.1016/j.cej.2014.09.017.
33. Miao Q, Li G (2021) Potassium phosphate/magnesium oxide modified biochars: Interfacial chemical behaviours and Pb binding performance. Sci Total Environ 759:143452. https://doi.org/10.1016/j.scitotenv.2020.143452.
34. Mohamed WR, Sami NM, Metwally SS, Saad EA (2022) Surface modification of ball clay minerals with gamma irradiation polymerization for removal of cerium and gadolinium ions from aqueous phase. Hydrometallurgy 208:105816. https://doi.org/10.1016/j.hydromet.2022.105816.
35. Mu S, Sun D, Liu Y, Li J, Zhang H, Wang J (2022) Ultraviolet-visible and fluorescence spectra indicate the binding and transformation properties of hexavalent chromium in DOM solution. J Environ Chem Eng 10:107158. https://doi.org/10.1016/j.jece.2022.107158.
36. Pillai SS, Mullassery MD, Fernandez NB, Girija N, Geetha P, Koshy M (2013) Biosorption of Cr(VI) from aqueous solution by chemically modified potato starch: Equilibrium and kinetic studies. Ecotoxicol Environ Saf 92:199–205. https://doi.org/10.1016/j.ecoenv.2013.01.020.
37. Qu X, Fu H, Mao J, Ran Y, Zhang D, Zhu D (2016) Chemical and structural properties of dissolved black carbon released from biochars. Carbon 96:759–767. https://doi.org/10.1016/j.carbon.2015.09.106.
38. Shen L, Wang Y, Liu R, Yang Y, Liu Y, Xing B (2023) Aging characteristics of degradable and non-biodegradable microplastics and their adsorption mechanism for sulfonamides. Sci Total Environ 901:166452. https://doi.org/10.1016/j.scitotenv.2023.166452.
39. Shen Z, Zhang Y, Jin F, McMillan O, Al-Tabbaa A (2017) Qualitative and quantitative characterisation of adsorption mechanisms of lead on four biochars. Sci Total Environ 609:1401–1410. https://doi.org/10.1016/j.scitotenv.2017.08.008.
40. Shi W, Zhang G, Li F, Feng J, Chen X (2020) Two-step adsorption model for Pb ion accumulation at the algae-water interface in the presence of fulvic acid. Sci Total Environ 742:140606. https://doi.org/10.1016/j.scitotenv.2020.140606.
41. Spessato L, Bedin KC, Cazetta AL, Souza IP, Duarte VA, Crespo LH, Silva MC, Pontes RM, Almeida VC (2019) KOH-super activated carbon from biomass waste: Insights into the paracetamol adsorption mechanism and thermal regeneration cycles. J Hazard Mater 371:499–505. https://doi.org/10.1016/j.jhazmat.2019.02.102.
42. Sucaldito MR, Camacho DH (2017) Characteristics of unique HBr-hydrolyzed cellulose nanocrystals from freshwater green algae (Cladophora rupestris) and its reinforcement in starch-based film. Carbohydr Polym 169:315–323. https://doi.org/10.1016/j.carbpol.2017.04.031.

43. Tan L, Ma Z, Yang K, Cui Q, Wang K, Wang T, Wu GL, Zheng J (2020) Effect of three artificial aging techniques on physicochemical properties and Pb adsorption capacities of different biochars, Sci. Total Environ 699:134223. https://doi.org/10.1016/j.scitotenv.2019.134223.
44. Teng C, Zhou K, Peng C, Chen W 203 (2021) Characterization and treatment of landfill leachate: A review, Water Res 117525. https://doi.org/10.1016/j.watres.2021.117525.
45. Teng Z, Shao W, Zhang K, Huo Y, Zhu J, Li M (2019) Pb biosorption by Leclercia adecarboxylata: Protective and immobilized mechanisms of extracellular polymeric substances. Chem Eng J 375:122113. https://doi.org/10.1016/j.cej.2019.122113.
46. Wang H, Liu R, Chen Q, Mo Y, Zhang Y (2022) Biochar-supported starch/chitosan-stabilized nano-iron sulfide composites for the removal of lead ions and nitrogen from aqueous solutions. Bioresour Technol 347:126700. https://doi.org/10.1016/j.biortech.2022.126700.
47. Wang L, Guo C, Qian Q, Lang D, Wu R, Abliz S, Wang W, Wang J (2023) Adsorption behavior of UV aged microplastics on the heavy metals Pb (II) and Cu (II) in aqueous solutions. Chemosphere 313:137439. https://doi.org/10.1016/j.chemosphere.2022.137439.
48. Wang Q, Zheng C, Shen Z, Lu Q, He C, Zhang TC, Liu J (2019) Polyethyleneimine and carbon disulfide co-modified alkaline lignin for removal of $Pb^{2+}$ ions from water. Chem Eng J 359:265–274. https://doi.org/10.1016/j.cej.2018.11.130.
49. Wang X, Jing Y, Cao Y, Xu S, Chen L (2019) Effect of chemical aging of Alternanthera philoxeroides-derived biochar on the adsorption of Pb(II). Water Sci Technol 80:329–338. https://doi.org/10.2166/wst.2019.276.
50. Wang Y, van Zwieten L, Wang H, Wang L, Li R, Qu J, Zhang Y (2022) Sorption of Pb(II) onto biochar is enhanced through co-sorption of dissolved organic matter. Sci Total Environ 825:153686. https://doi.org/10.1016/j.scitotenv.2022.153686.
51. Wang Z, Liu G, Zheng H, Li F, Ngo HH, Guo W, Liu C, Chen L, Xing B (2015) Investigating the mechanisms of biochar's removal of lead from solution. Bioresour Technol 177:308–317. https://doi.org/10.1016/j.biortech.2014.11.077.
52. Wen Z, Shang Y, Song K, Liu G, Hou J, Lyu L, Tao H, Li S (2022) Composition of dissolved organic matter (DOM) in lakes responds to the trophic state and phytoplankton community succession. Water Res 224:119073. https://doi.org/10.1016/j.watres.2022.119073.
53. Wu J, Wang T, Wang J, Zhang Y, Pan WP (2021) A novel modified method for the efficient removal of Pb and Cd from wastewater by biochar: Enhanced the ion exchange and precipitation capacity. Sci Total Environ 754:142150. https://doi.org/10.1016/j.scitotenv.2020.142150.
54. Wu J, Wang T, Zhang Y, Pan WP (2019) The distribution of Pb (II)/Cd (II) adsorption mechanisms on biochars from aqueous solution: Considering the increased oxygen functional groups by HCl treatment. Bioresour Technol 291:121859. https://doi.org/10.1016/j.biortech.2019.121859.
55. Xie PP, Deng JW, Zhang HM, Ma YH, Cao DJ, Ma RX, Liu RJ, Liu C, Liang YG (2015) Effects of cadmium on bioaccumulation and biochemical stress response in rice (Oryza sativa L.). Ecotoxicol Environ Saf 122:392–398. https://doi.org/10.1016/j.ecoenv.2015.09.007.

56. Xue Z, Guo J, Wu S, Xie W, Fu Y, Zhao X, Fan K, Xu M, Yan H, Shao M, Duan X (2023) Co-thermal in-situ reduction of inorganic carbonates to reduce carbon-dioxide emission. Sci China Chem 66:1201–1210. https://doi.org/10.1007/s11426-022-1537-6.
57. Yan M, Dryer D, Korshin GV, Benedetti MF (2013) In situ study of binding of copper by fulvic acid: Comparison of differential absorbance data and model predictions. Water Res 47:588–596. https://doi.org/10.1016/j.watres.2012.10.020.
58. Yang Y, Wei Z, Zhang X, Chen X, Yue D, Yin Q, Xiao L, Yang L (2014) Biochar from Alternanthera philoxeroides could remove Pb (II) efficiently. Bioresour Technol 171:227–232. https://doi.org/10.1016/j.biortech.2014.08.015.
59. Yuan W, Kuang J, Yu M, Huang Z, Zou Z, Zhu L (2021) Facile preparation of MoS2@Kaolin composite by one-step hydrothermal method for efficient removal of Pb(II). J Hazard Mater 405:124261. https://doi.org/10.1016/j.jhazmat.2020.124261.
60. Zafar R, Bang TH, Lee YK, Begum MS, Rabani I, Hong S, Hur J (2022) Change in adsorption behavior of aquatic humic substances on microplastic through biotic and abiotic aging processes. Sci Total Environ 843:157010. https://doi.org/10.1016/j.scitotenv.2022.157010.
61. Zhang H, Geng G, Jun-jie W, Xin Y, Zhang Q, De-ju C, You-hua M (2019) The remediation potential and kinetics of cadmium in the green alga Cladophora rupestris. Environ Sci Pollut Res 26:775–783. https://doi.org/10.1007/s11356-018-3661-z.
62. Zhang L, Feng X, Qiu C, Li L, Sun Y, Tao X, Li X, Liu Z, Cao D (2024) The remediation potential and kinetics of $Pb^{2+}$ adsorbed by the organic frameworks of Cladophora rupestris. Environ Sci Pollut Res 1–13. https://doi.org/10.1007/s11356-024-32029-2.
63. Zhang P, Shao Y, Xu X, Huang P, Sun H (2020) Phototransformation of biochar-derived dissolved organic matter and the effects on photodegradation of imidacloprid in aqueous solution under ultraviolet light. Sci Total Environ 724:137913. https://doi.org/10.1016/j.scitotenv.2020.137913.
64. Zhang T, Zhu X, Shi L, Li J, Li S, Lü J, Li Y (2017) Efficient removal of lead from solution by celery-derived biochars rich in alkaline minerals. Bioresour Technol 235:185–192. https://doi.org/10.1016/j.biortech.2017.03.109.
65. Zhang Y, Wang Y, Zhang X, Li R, Chen Y, Meng Q (2017) Investigating the behavior of binding properties between dissolved organic matter (DOM) and Pb(II) during the soil sorption process using parallel factor analysis (PARAFAC) and two-dimensional correlation spectroscopy (2D-COS). Environ Sci Pollut Res 24:25156–25165. https://doi.org/10.1007/s11356-017-0167-z.
66. Zhang Y, Yue X, Xu W, Zhang H, Li F (2019) Amino modification of rice straw-derived biochar for enhancing its cadmium (II) ions adsorption from water. J Hazard Mater 379:120783. https://doi.org/10.1016/j.jhazmat.2019.120783.
67. Zhao H, Zhang C, Liu G, Li J, Yang B, Ma H, Zhang X, Wang D (2022) Crosslinking of Trans-1, 4-polyisoprene by γ-ray radiation. Polym Degrad Stab 197:109869. https://doi.org/10.1016/j.polymdegradstab.2022.109869.

68. Zhao R, Wang B, Wu P, Feng Q, Chen M, Zhang X, Wang S (2023) Calcium alginate-nZVI-biochar for removal of Pb/Zn/Cd in water: Insights into governing mechanisms and performance. Sci Total Environ 894:164810. https://doi.org/10.1016/j.scitotenv.2023.164810.
69. Zhou X, Hou Z, Song J, Lv L (2020) Spectrum evolution of dissolved aromatic organic matters (DAOMs) during electro-peroxi-coagulation pretreatment of coking wastewater. Sep Purif Technol 235:116125. https://doi.org/10.1016/j.seppur.2019.116125.
70. Zhu K, Jia H, Sun Y, Dai Y, Zhang C, Guo X, Wang T, Zhu (2020) Long-term phototransformation of microplastics under simulated sunlight irradiation in aquatic environments: Roles of reactive oxygen species. Water Res 173:115564. https://doi.org/10.1016/j.watres.2020.115564.
71. Zhu K, Jia H, Zhao S, Xia T, Guo X, Wang T, Zhu L (2019) Formation of environmentally persistent free radicals on microplastics under light irradiation. Environ Sci Technol 53:8177–8186. https://doi.org/10.1021/acs.est.9b01474.
72. Zhu L, Yu B, Chen H, Yu J, Yan H, Luo Y, He J, Huang Z, Zheng P, Mao X (2022) Luo J Comparisons of the micronization, steam explosion, and gamma irradiation treatment on chemical composition, structure, physicochemical properties, and in vitro digestibility of dietary fiber from soybean hulls. Food Chem 366:130618. https://doi.org/10.1016/j.foodchem.2021.130618.
73. Zulkifly S, Hanshew A, Young EB, Lee P, Graham ME, Graham ME, Piotrowski M, Graham LE (2012) The epiphytic microbiota of the globally widespread macroalga Cladophora glomerata (Chlorophyta, Cladophorales). Am J Bot 99:1541–1552. https://doi.org/10.3732/ajb.1200161.

# Figures

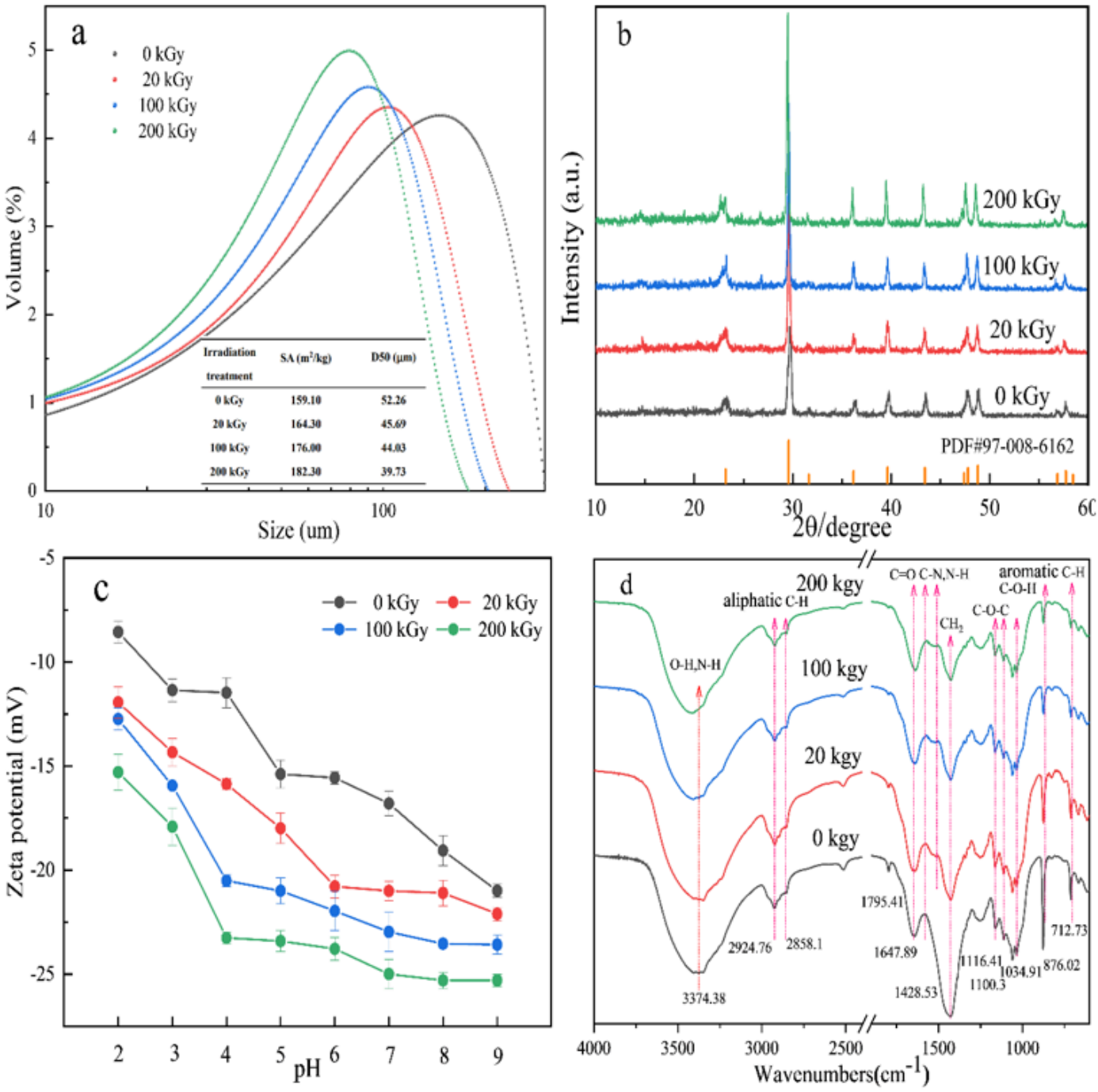


## Figure 2

(a) Particle size distribution, (b) XRD, (c) zeta potential, and (d) FTIR of *C. rupestris* biomass treated with different $^{60}$Coγ–ray irradiation doses

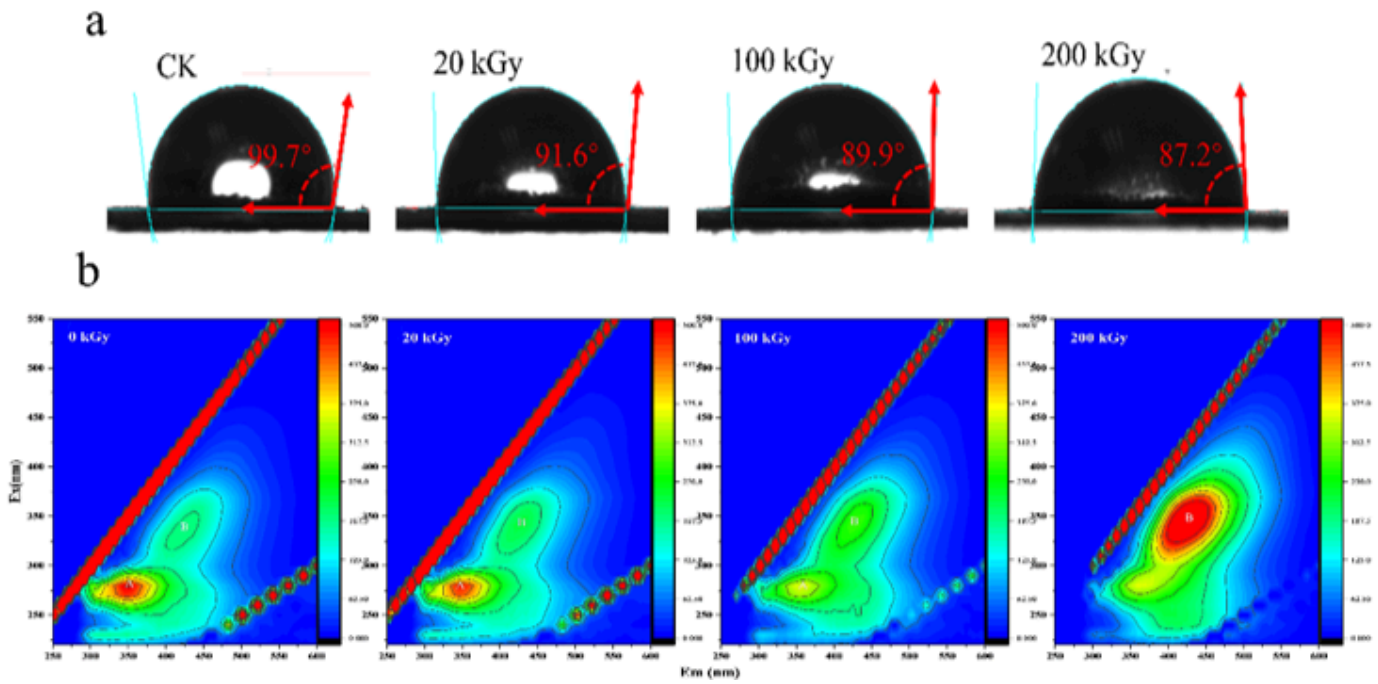


**Figure 3**

(a) Water contact angle and (b) 3D-EEM spectra of DOM from *C. rupestris* biomass treated with different $^{60}$Coγ–ray irradiation doses

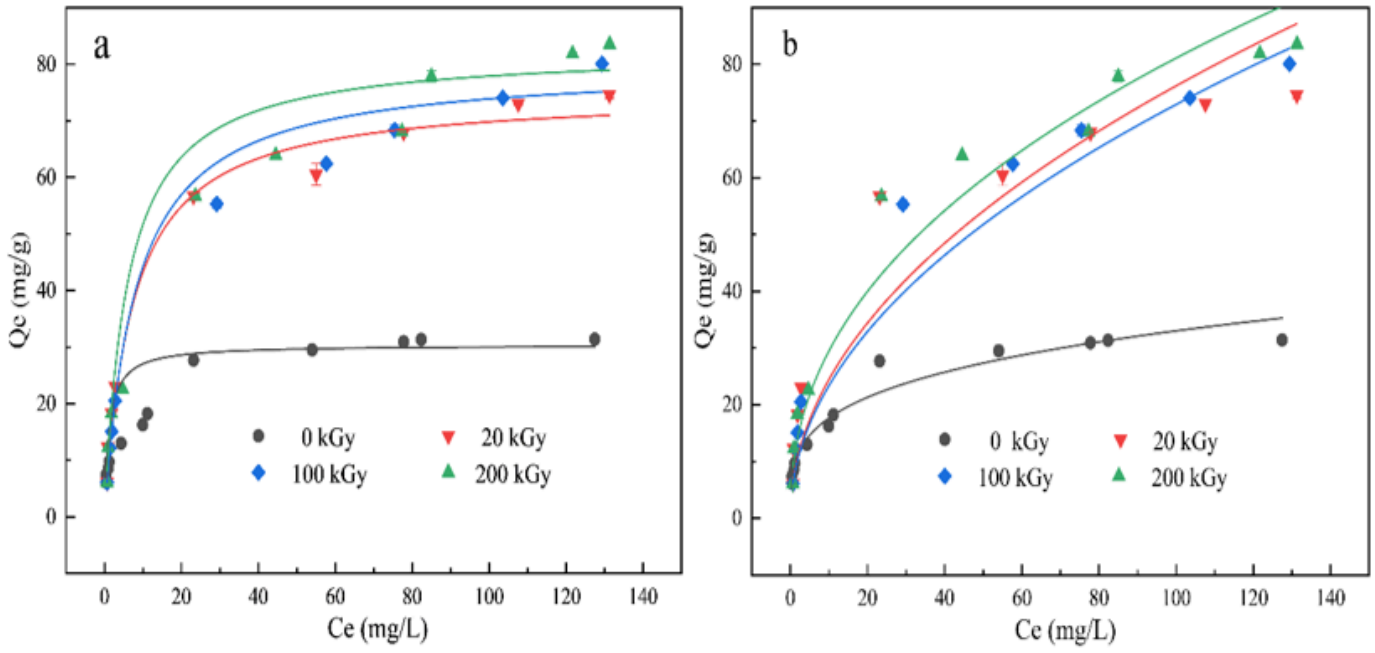


**Figure 4**

(a) Langmuir and (b) Freundlich isotherms of $Pb^{2+}$ on the *C. rupestris* biomass treated with different $^{60}Co\gamma$–ray irradiation doses

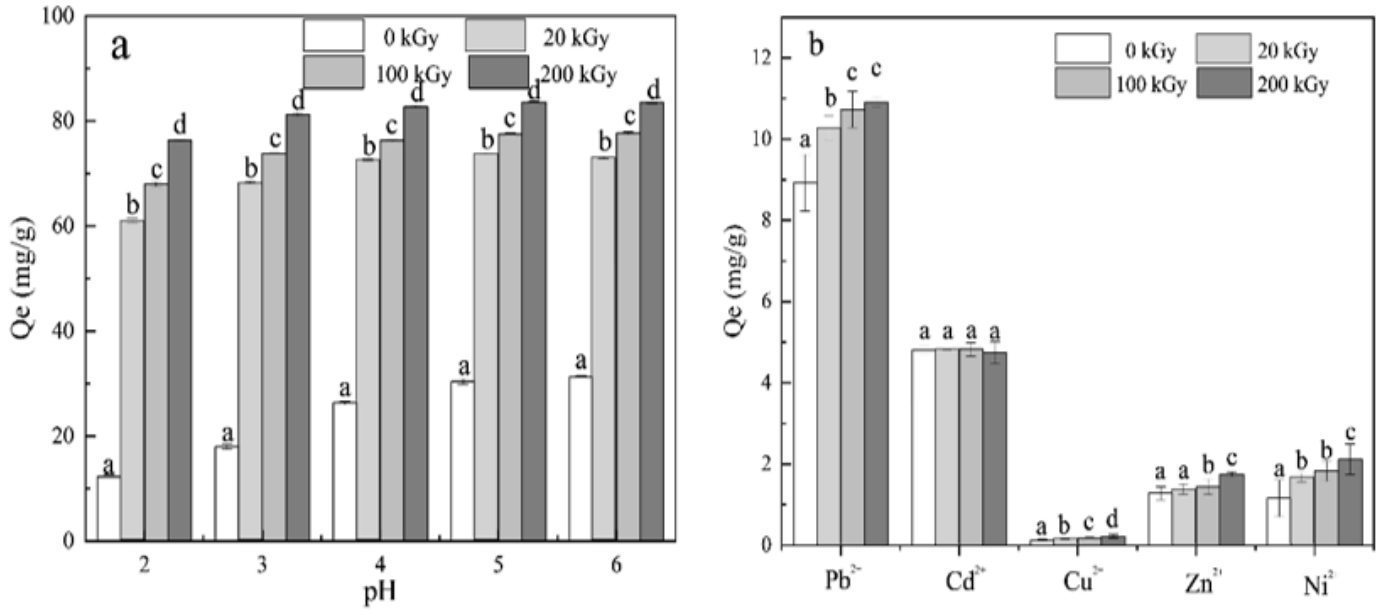


## Figure 5

(a) Influence of initial pH and (b) co−existing ions on $Pb^{2+}$ adsorption for *C. rupestris* biomass treated with different $^{60}Co\gamma$–ray irradiation doses

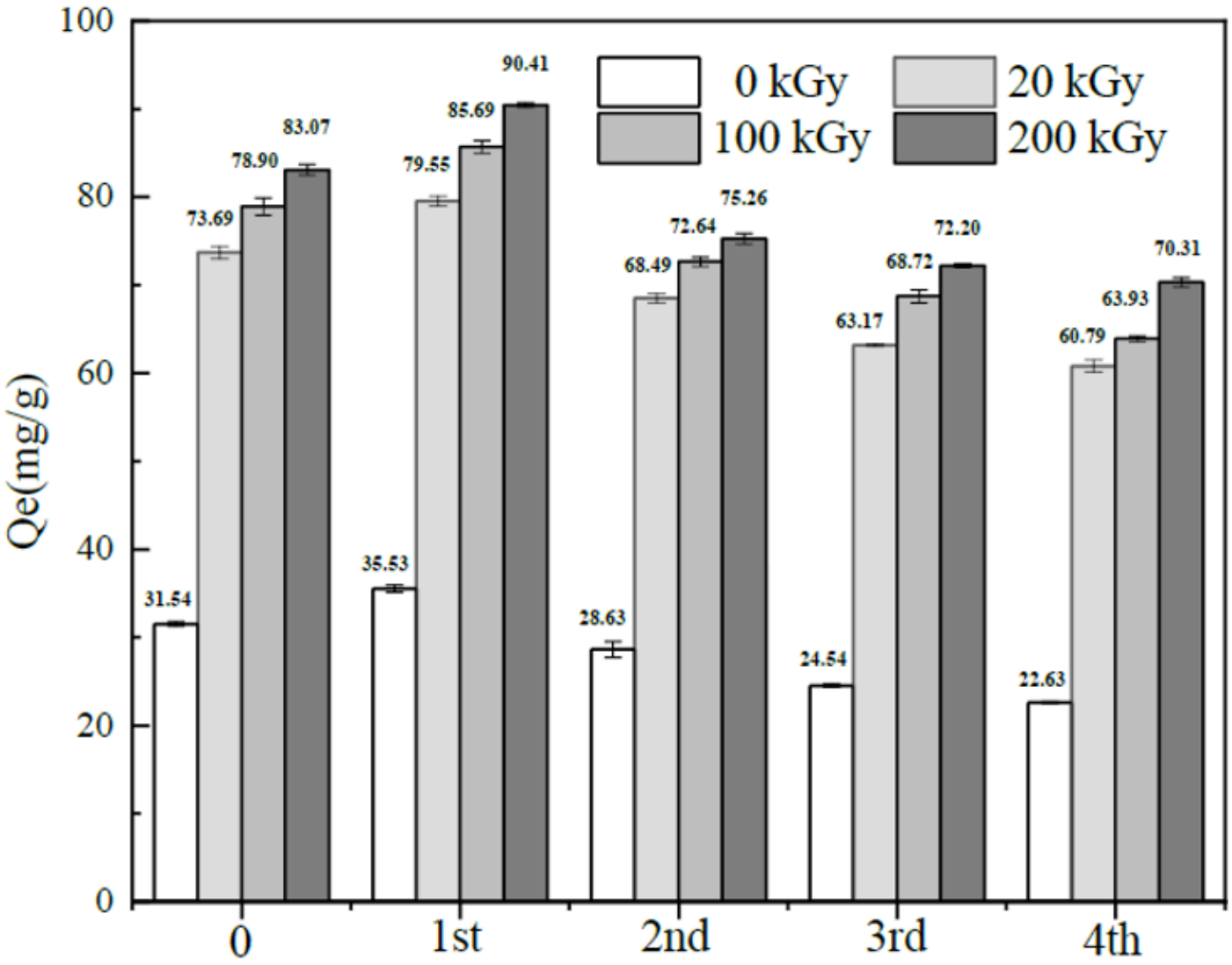


**Figure 6**

Adsorption efficiency of *C. rupestris* biomass samples irradiated by $^{60}$Coγ-rays on $Pb^{2+}$ adsorption for four consecutive adsorption/desorption cycles

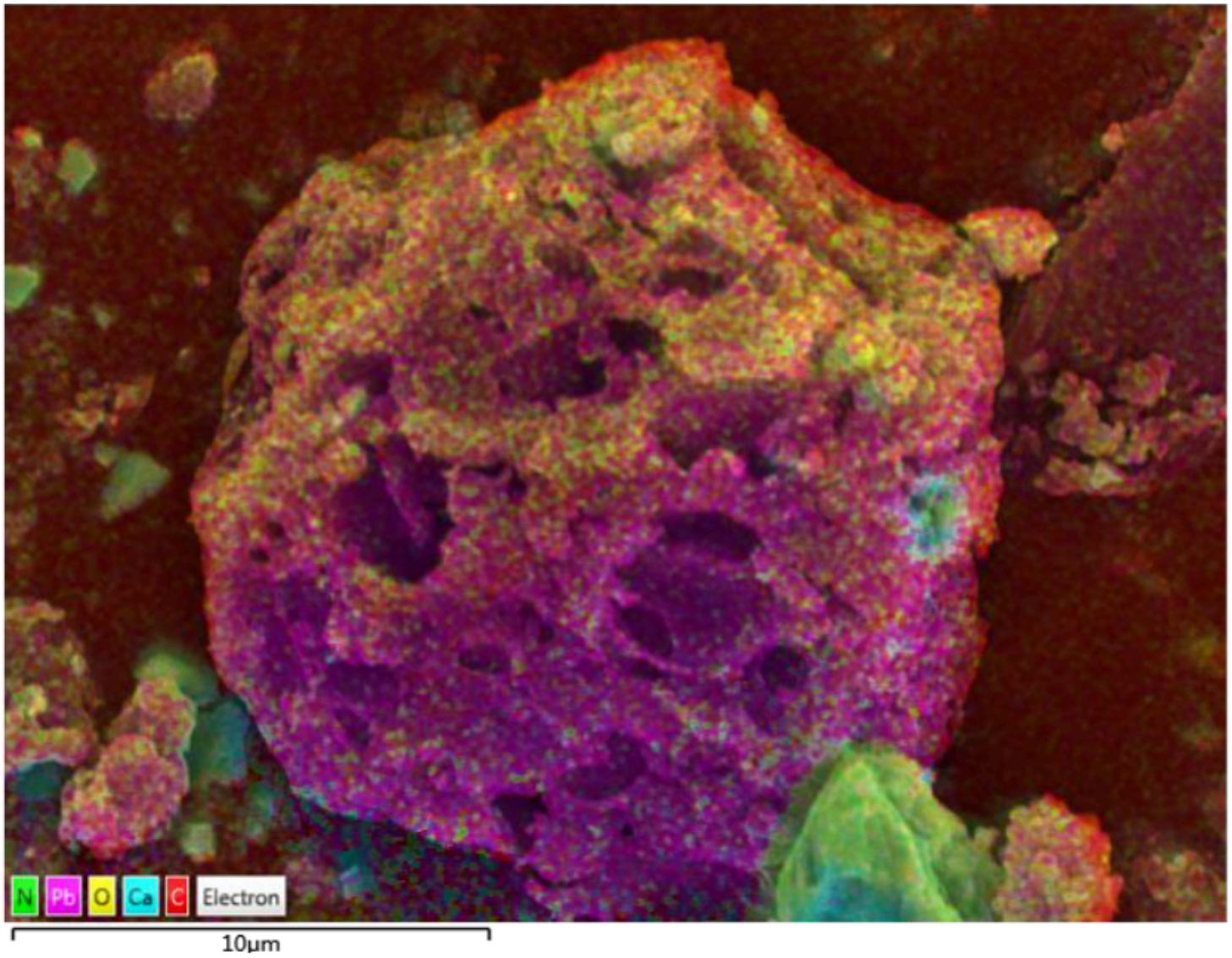


## Figure 7

SEM-EDS spectrum of *C. rupestris biomass* samples irradiated by $^{60}$Coγ-rays after adsorption of $Pb^{2+}$

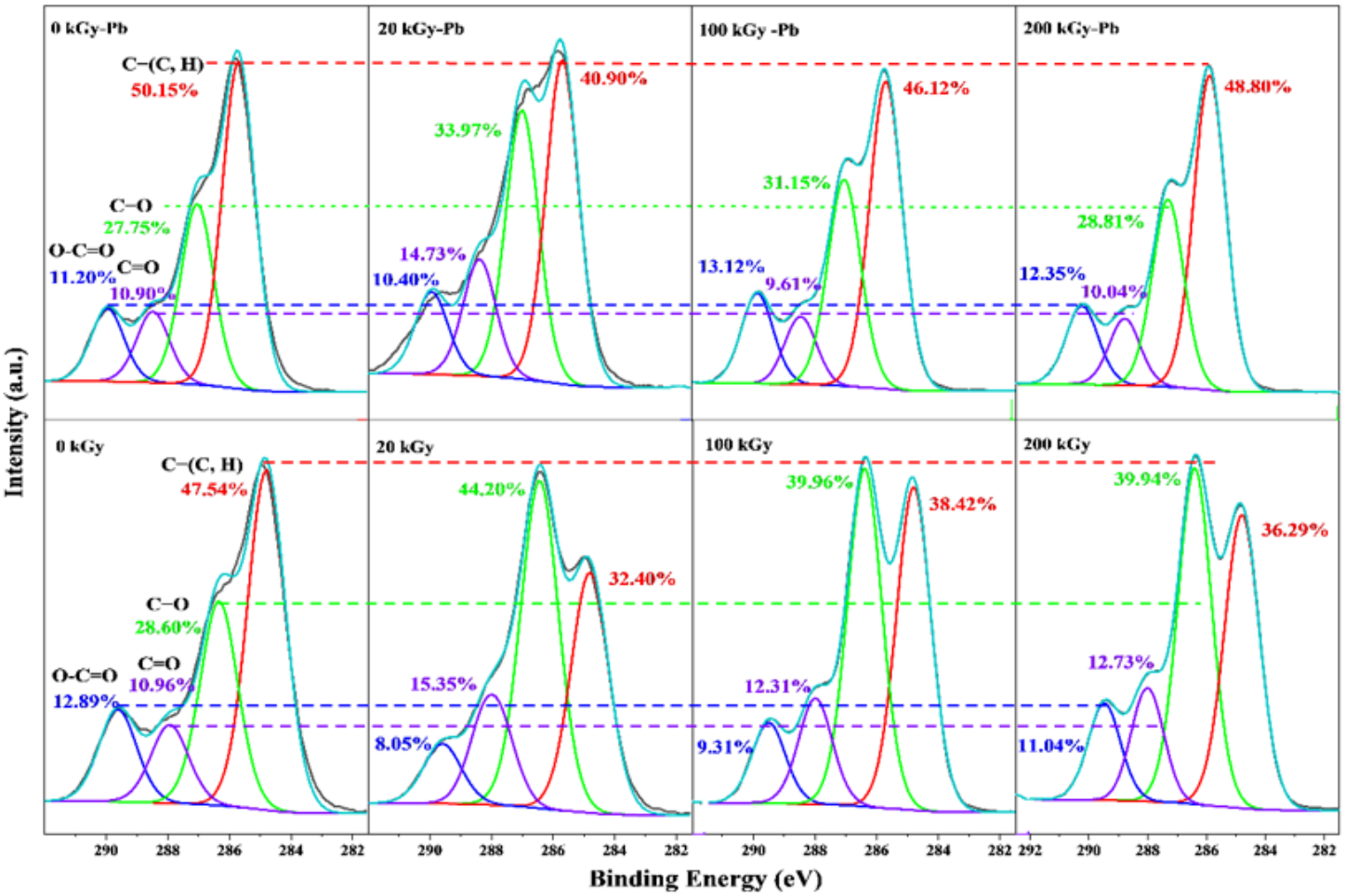


## Figure 8

C 1s spectra of *C. rupestris* biomass samples irradiated by $^{60}$Coγ-ray before (above) and after (below) adsorption of $Pb^{2+}$

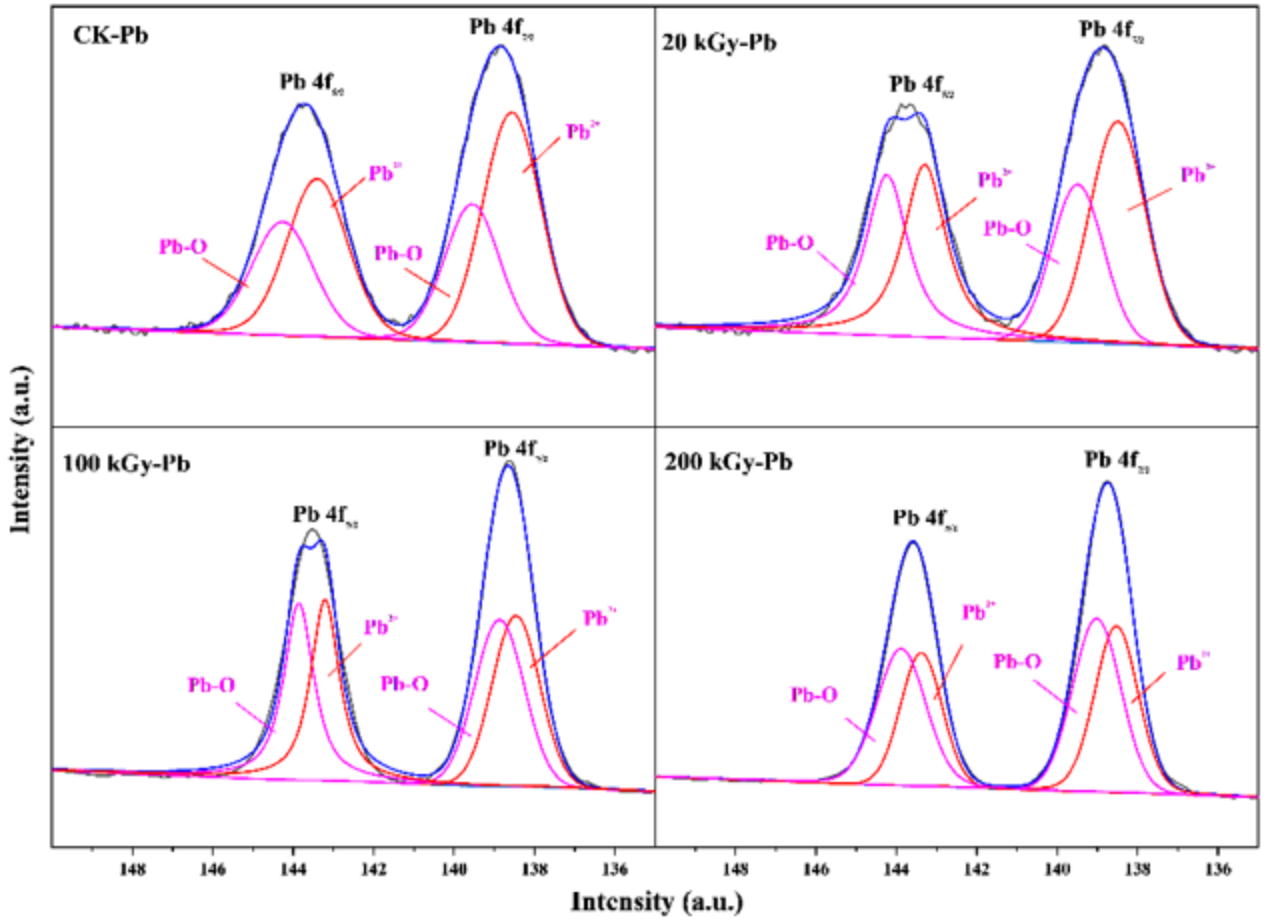


## Figure 9

Pb 4f7/2 and Pb 4f5/2 spectra of *C. rupestris* biomass treated with different $^{60}$Coγ–ray irradiation doses

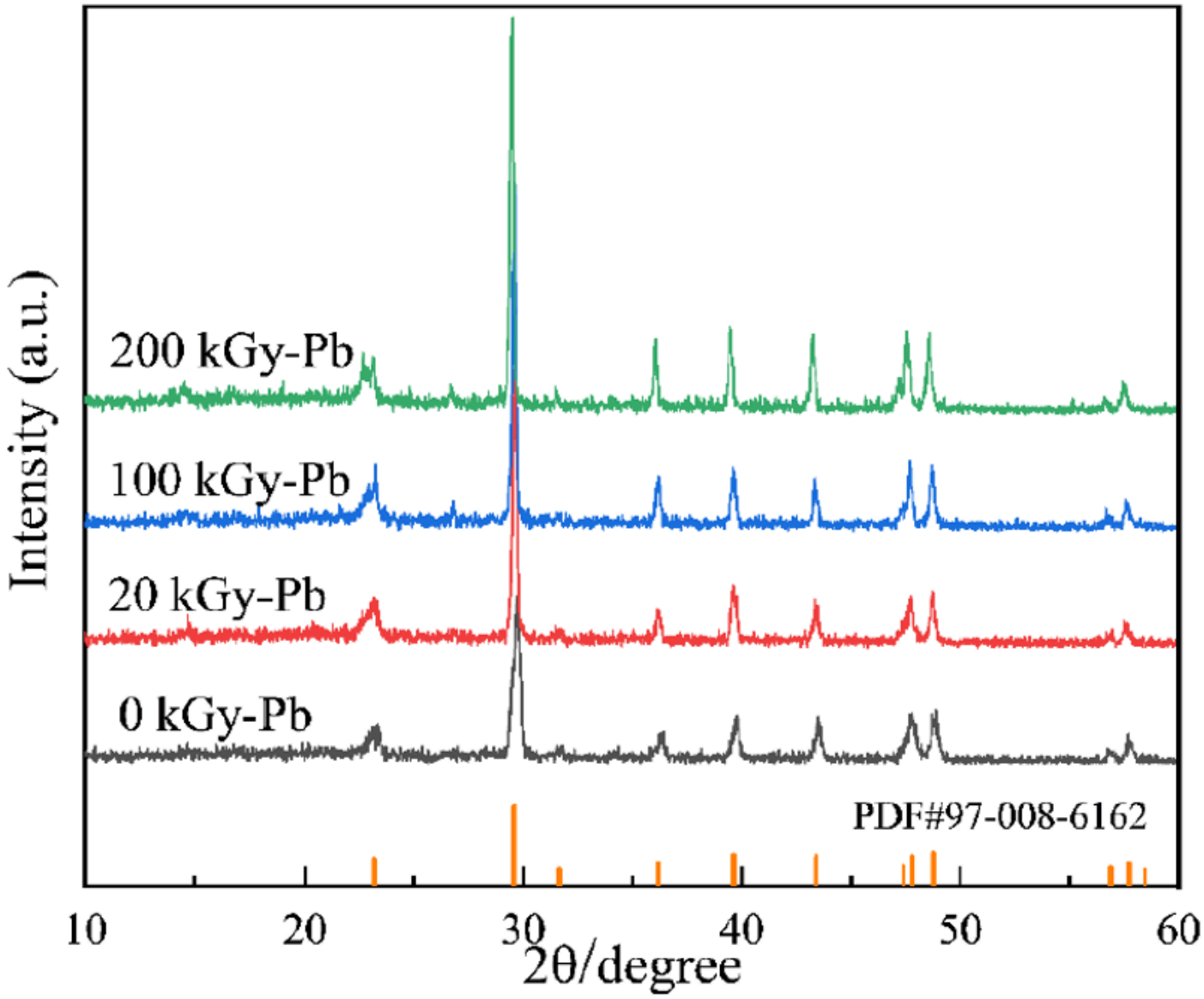


**Figure 10**

XRD of *C. rupestris* biomass samples irradiated by $^{60}$Coγ-ray after adsorption of $Pb^{2+}$

## Supplementary Files

This is a list of supplementary files associated with this preprint. Click to download.

- GraphicalAbstract.png
- SupplementaryMaterials.docx